UNIVERSITY OF CALIFORNIA

SANTA CRUZ

Plasmonic Zero Waveguide Modes and Radiative Decay Engineering of Quantum Emitters

A thesis submitted in partial satisfaction
of the requirements for the degree of

MASTER OF SCIENCE

in

ELECTRICAL ENGINEERING

by

DAVID COTA GONZALEZ

December 2015

The Thesis of David Cota Gonzalez
is approved:

_____

Professor Ahmet Ali Yanik, Chair

_____

Professor Joel Kubby

_____

Professor Nader Pourmand

_____

Tyrus Miller
Vice Provost and Dean of Graduate Studies

Table of Contents

List of Figures

List of Tables

Abstract

Plasmonic Zero Waveguide Modes and Radiative Decay Engineering of Quantum Emitters

by

David Cota Gonzalez

This paper documents an investigation of plasmonic behavior and the application of plasmonic phenomena with the intended purpose of fabricating and manufacturing a novel zero-mode waveguide (ZMW). The conventional ZMW can focus incident light to tiny volumes on the order of zeptoliters (zL) in magnitude. This ability to focus light beyond the diffraction limit is promising for single molecule detection (SMD) particularly when investigating a sample of μM concentrations or beyond. While the prospect of having the excitation light intensity focused to zL volumes is desirable for SMD, the observer still requires that the intensity of light emissions from the molecule under investigation be sufficiently larger than the noise from the excitation light source, any fluorophores beyond the observation volume and other light emissions which may disrupt the sample study. The solutions under investigation may be susceptible to quenching; thus, the waveguide must be designed so as to apply a maximum intensity into a volume of minimal size all while detecting the enhanced emissions without damaging the sample.

A conventional ZMW consisting of a 50nm diameter cylindrical etch of a 100nm thick Aluminum (Al) metal film lying atop a glass substrate produces zL-effective observation volumes.[16] We proceeded to design and simulate ZMW structures consisting of two or more metallic columns standing in a rectangular etch of a heterogeneous stack — Gold and Aluminum — atop a glass substrate. The waveguide takes advantage of plasmonic devices' capacity to both confine light and also enhance the fluorescence signal emanating from the confined volume.

Dedication

For you Nini. I miss you.

Acknowledgements

I would like to thank Xiangchao Zhu, or Jude as I know him. For working so hard by my side, for pushing me, for demanding results, for asking the tough questions, for letting me figure things out, for all the time he spent making sure I understood what I was doing.

I would like to thank Dr. Ahmet Ali Yanik for guiding Jude and I, and for providing me with an opportunity to do research. Thank you for all your support and wisdom.

I would like to thank the Electrical Engineering department at UC Santa Cruz. There are too many individuals to mention, all the fellow graduate students, staff, faculty, those who made sure we had warm coffee and clean wastebaskets, the undergraduates who I TA'd and to Juan José Díaz León and Jinbo Zhu for TAing by my side.

I would like to thank the Hispanic Scholarship Fund and Google Scholars for helping me fund my studies.

I would like to thank Liz, Fabian, Valentina, and the other little one on the way. For challenging me in ways that a classroom, laboratory nor computer simulation could match. For loving me. For allowing me to be a part of your lives, for being a part of my life. I love you guys.

To my family, thank you. For always accepting and loving me in all my ways. For being by my side since the day I was born.

1 Introduction

In classical electromagnetics it is perceived that the incident energy will be fully absorbed or reflected when interacting with a metal. The character of the electrons within the metal, however, more accurately exhibit wavelike behaviors much akin to propagating waves in bodies of water. The motion of this sea of electrons within the metal has been described by the *plasma model*.[18] This sea of electrons may produce surface plasmon polaritons (SPP) which are electromagnetic excitations at the interface between the metal and a dielectric medium. For a metal with plasma frequency ω_p, we will be focusing on two phenomena for our ZMW design: (i) when an electromagnetic signal of frequencies ω which is lower than the plasma frequency $\omega_p > \omega$ $(\lambda_p < \lambda)$ the electromagnetic signal will penetrate the metal a distance δ called the skin depth; and (ii) for frequencies ω equivalent to or larger than the plasma frequency $\omega_p \leq \omega$ $(\lambda_p \geq \lambda)$, the energy will experience an increased damping.[18] When the dimension a of the metal is comparable to the skin depth $\delta \approx a$ an evanescent tail of energy will evacuate the metal along the direction of propagation resulting from the electron sea interactions with the incident energy.[14] Also, when the wavelength of incidence λ is comparable to a metal's plasma wavelength $\lambda_p \approx \lambda$ the optical cross-section of the metal may be much larger than the geometric cross-section of the metal which will result in an energy enhancement in the vicinity of the nanoparticles.[14]

Upon a competent understanding of the plasma model and a benchmarking of previous studies, we move forward to design novel devices integrating plasmonics with ZMWs for strong confinement and enhanced fluorescence. Simulations were run and documented for nanoparticle cross-sections, fluorescence enhancement and radiation patterns. Integration of surface plasmonics may lead to the fabrication and testing of novel ZMWs with characteristics of sub-zeptoliter excitation volumes, near-field intensity enhancements 170 times or stronger than those of the conventional ZMW as well as fluorescence emission rates larger than those of a molecule in free-space.[28] Potential applications of zL optical excitation volumes which also exhibit a fluorescence emission enhancement include macromolecule investigation, cell imaging, and

DNA sequencing.[14] Past laboratory experiments have shown that finite-difference time-domain (FDTD) simulations could be used for precise engineering of ZMWs and enable designs with increased usable sample concentration ranges by well over three orders of magnitude and a temporal resolution an order of magnitude faster than conventional diffraction limited approaches.[16] Using the same simulation conditions — solely changing the structure from a conventional ZMW (Fig. 15d) to our custom heterogeneous stack ZMW with custom etch (Fig. 27) — a conventional ZMW with an enhancement factor of ≈ 1.8 while the enhancement factor of our custom design was ≈ 22. We hope to further our study and investigate the signal-to-noise ratio (SNR) of the different structures and also to obtain quantitative results for the excitation volumes of potential structures.

This thesis is organized as follows. First, an introduction to plasmonics followed by an overview of the physics of fluorescence light generation will be presented. A discussion on the use of the FDTD method to solve Maxwell's equations and understand excitation and emission enhancements without using any fitting parameters. To verify the validity and proper use of time domain simulations, we present methods and benchmark previously published work using our own method. Once we are assured with the validity of our simulations, we move forward to design novel structures showing enhanced device characteristics beyond the conventional ZMWs.

2 Background

In this section, a brief introduction on the different optical models will be presented followed by a recap of electromagnetics which will aid in the transition to plasmonics. The physics of fluorescence, the fluorescence enhancement of metals and the analysis method fluorescence correlation spectroscopy (FCS) follows. The FDTD method and solutions will be given subsequently.

2.1 Electromagnetics

There are currently four different models used to physically describe light; those models being the ray, wave, electromagnetic and the quantum models. The specific

optical model of the four one would use depends on the complexity of the application at hand.

The least mathematically complex of these optics models, which also happens to be the oldest model and the foundation of the physical representation of light, is the classical approach. The classical view interprets the photon's behavior as that of a ray. A more encompassing understanding of a photon is the wave approach (a unique wave of interest is the Gaussian beam which is an important solution to the paraxial *Helmholtz equation*[1]). The wave model interprets the photon as a wave traveling through space and time, much like a wave traversing through the a body of water. The wave modeling of light mathematically explains phenomena such as diffraction and resonance (or constructive interference).

A more accurate model of the photon character is the electromagnetic representation of the photon, which stems from the studies of James Clerk Maxwell. Maxwell's work led to, amongst other things, the naming of a collection of four differential equations which describe classical electrodynamics as Maxwell's equations (Eq.1a-d). Maxwell's equations are Gauss's Law (Eq.1a), Gauss's Law for Magnetism (Eq.1b), Faraday's Law (Eq.1c) and the Ampère-Maxwell Law (Eq.1d).

$$\boldsymbol{\nabla} \cdot \boldsymbol{D} = \rho \tag{1a}$$

$$\boldsymbol{\nabla} \cdot \boldsymbol{B} = 0 \tag{1b}$$

$$\boldsymbol{\nabla} \times \boldsymbol{E} = -\frac{\partial \boldsymbol{B}}{\partial t} \tag{1c}$$

$$\boldsymbol{\nabla} \times \boldsymbol{H} = \boldsymbol{J} + \frac{\partial \boldsymbol{D}}{\partial t} \tag{1d}$$

The most mathematically accurate physical model of the photon at the current time and space of this writing is the quantum optics model, which explains that the photon has a wave-particle like duality and that the energies at which a particle can emit and absorb photons is quantized. One can think of analog and digital signals as an analogy. In an analog signal the wave appears to be continuous (an infinite amount of values to represent the information) and in a digital signal there appears to be

[1] The *Helmholtz equation* being: $\boldsymbol{\nabla}^2 \cdot \boldsymbol{E} + k_0^2 \varepsilon \boldsymbol{E} = 0$

a step with infinite slope at each sample in the wave (the information in the wave wave is constructed from a limited and specific set of values, or quanta, determined by a limited number of ones and zeros utilized to represent the information).

2.2 Plasmonics

As it pertains to the studies undertaken in this paper, we are primarily concerned with the infrared (IR), visible and ultraviolet (UV) regions of the electromagnetic spectrum. The IR spectrum includes wavelength λ ranges from 760nm up to one micron. The visible spectrum ranges between values of 390nm and 760nm for λ and the UV spectrum encompasses wavelength λ values between 390nm down to 10nm. The material of this paper will also make extensive use of Maxwell's equations. Equation 2 describes the relationship between relative permittivity ε and conductivity σ of a material.[18]

$$\varepsilon(\boldsymbol{K}, \omega) = 1 + \frac{i\sigma(\boldsymbol{K}, \omega)}{\varepsilon_0 \omega} \tag{2}$$

The relationship between the complex index of refraction $\widetilde{n}$ of a material and said material's relative permittivity, or *dielectric function*, ε is defined as $\widetilde{n} = \sqrt{\varepsilon}$. Where the complex index of refraction $\widetilde{n}$ is

$$\widetilde{n}(\omega) = n(\omega) + i\kappa(\omega) \tag{3}$$

The real part of the complex index of refraction $\widetilde{n}$ is the index of refraction n and the imaginary part is the extinction coefficient κ. The extinction coefficient κ of a material determines the optical absorption of the material when electromagnetic waves are propagating through the medium. The absorption coefficient α from Beer's law is related to κ by

$$\alpha(\omega) = \frac{2\kappa(\omega)\omega}{c} \tag{4}$$

Conductivity σ, the extinction coefficient κ, and the absorption coefficient α are not to be confused with the cross-sections (σ_{sca}, σ_{ext} and σ_{abs}) of a material.[18][23]
The sea of electrons in the metal will oscillate in response to the electromagnetic signals attempting to propagate through the metal. The *plasma frequency* ω_p of the

free electron gas in a metal is

$$\omega_p^2 = \frac{ne^2}{\varepsilon_0 m} \tag{5}$$

The metal here has an effective optical mass m and ε_0 is the electric permittivity in a vacuum (Appendix 7.1). The dielectric function of the free electron gas can then be written as

$$\varepsilon(\omega) = 1 - \frac{\omega_p^2}{\omega^2 + i\gamma\omega} \tag{6}$$

Where γ is the collision frequency the electrons experience as they oscillate.

When the frequency of the electromagnetic signal is less than the plasma frequency of the metal, $\omega < \omega_p$, the metal is mainly absorbing due to the real and imaginary parts of the complex refractive index $\widetilde{n}$ being comparable in magnitude ($|n| \approx |\kappa|$).

The discussion on plasmonics until this point has focused on bulk, or *volume*, plasmons. The work done in this paper, however, will exploit the effects due to the two types of plasmons found at or along the surface of a metal so as to achieve resonance of the optical signal: *surface plasmon polaritons* (SPPs) and *localized surface plasmons* (LSPs or *localized plasmons*).

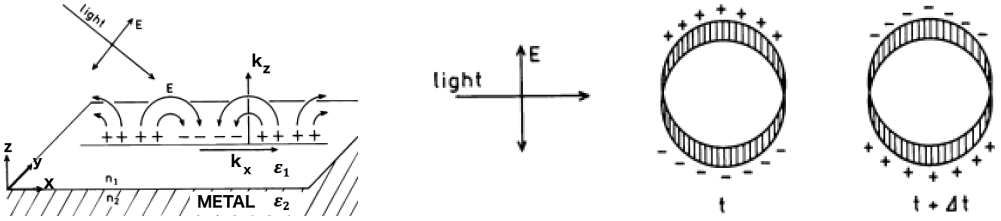

(a) SPPs (b) LSPs

Figure 1: **Surface Plasmons**. (a) propagating along the surface, SPPs and (b) localized surface plasmons.[13]

SPPs are evanescently confined electromagnetic excitations propagating at the interface between a dielectric and a conductor (Fig. 1a).[18] Surface modes are present for $\omega < \omega_p$ only for transverse magnetic (TM) polarizations, meaning the electric field is perpendicular to the direction of propagation. SPPs cannot be excited directly by light but they can be generated through the use of phase matching techniques (prism coupling as in the Kretschmann and Otto configurations or with periodic structures).[18] Localized plasmons on the other hand do not require special phase

matching techniques and can be excited by the illumination of direct light upon metals of sub-wavelength dimensions (Fig. 1b).

2.3 Fluorescence

Fluorescence may occur when a substance emits light due to energy loss of electronically excited states. The other type of light emission due to energy loss of electronically excited states is phosphorescence (Fig. 2a). A simplified Jablonski diagram (Fig. 2b) will aid in viewing and describing the fluorescence process.

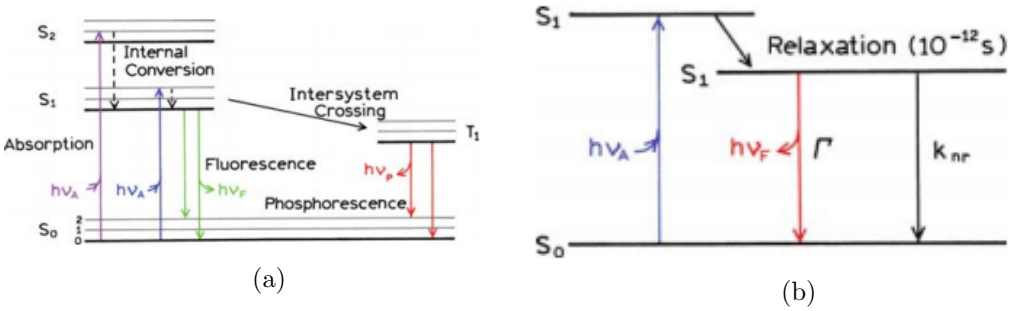

(a) (b)

Figure 2: **Jablonski Diagrams**. An example (a) Jablonski diagram demonstrating, among other processes, fluorescence and phosphorescence with the singlet ground, first, second and first triplet energy states depicted as S_0, S_1, S_2, and T_1, respectively, and (b) an example of a simplified Jablonski diagram.[15]

The blue lines of Fig. 2b symbolize an incident photon of energy $h\nu_A$ absorbed by an electron at the ground state energy level S_0 to a higher energy level S_1. In this simplified scenario, the excited electron first loses a fraction of it's energy after a relaxation time of about 1 ps (10^{-12} s). Following relaxation, the excited electron either decays by an energy $h\nu_F$ back to the ground state through non-radiative channels (k_{nr}, black vertical line) or as fluorescence emission (Γ, red vertical line). The quantum efficiency Q_f of this fluorophore depends on the radiative and non-radiative decay rates, Γ and k_{nr}, respectively, as:

$$Q_f = \frac{\Gamma}{\Gamma + k_{nr}} \tag{7a}$$

$$\tau_f = \frac{1}{\Gamma + k_{nr}} \tag{7b}$$

The quantum efficiency Q_f is a numerical representation of the number of emitted

photons to absorbed photons. The denominator of the internal quantum efficiency Q_f is the inverse of the lifetime τ_f (units of seconds) of the fluorophore. In this situation, the non-radiative decay rate would ideally be much smaller than the emission rate ($k_{nr} << \Gamma$) resulting in an internal quantum efficiency $Q_f = 1$. A decrease in fluorophore lifetime τ_f occurs for an increase in either Γ or k_{nr}. A decrease in k_{nr} without a change in emission rate Γ also leads to a decrease in quantum efficiency Q_f.

2.3.1 Excitation and Emission Enhancement

An optical system may be engineered in order to intensify the detected emissions from a radiating fluorophore with no change needed to the number of incident photons from source. The emitting fluorophore behaves as a radiating antenna, an oscillating dipole, but at high frequencies and short wavelengths. Plasmons at the surface of a metal can increase the total excitation and emission rates, E_T and Γ_T, respectively, of radiative decay when coupled with the radiating dipole.

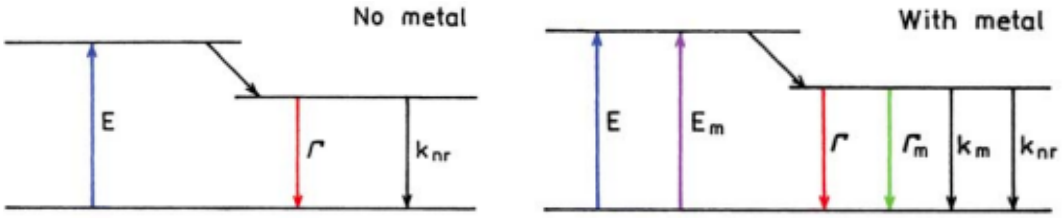

(a) (b) MEF

Figure 3: **Metal-Enhanced Fluorescence Jablonski Diagram**. Jablonski diagrams of (a) simplified diagram and (b) MEF simplified diagram.[15]

The metal-enhanced fluorescence (MEF) system will have increased rates of excitation E_m and emission Γ_m (Fig. 3). The accumulation of more fluorophore electrons in an excited state due an increased excitation rate included with an amplification of the rate of radiation leads to a higher probability of light emission.

$$Q_T = \frac{\Gamma + \Gamma_m}{\Gamma + \Gamma_m + k_{nr} + k_m} \tag{8a}$$

$$\tau_T = \frac{1}{\Gamma + \Gamma_m + k_{nr} + k_m} \tag{8b}$$

The MEF total lifetime τ_T is less than that of the metal-free fluorophore (τ_f) due to the inclusion of the two decay rates Γ_m and k_m. However, a decrease in total lifetime τ_T is not indicative of a smaller total quantum efficiency Q_T.

MEF systems can take advantage of a light source with lower incident intensity which would then require less energy to operate, produce lower background noise and may also prevent photobleaching since less intensity is applied to the fluorophores. The metal can also be manufactured in a unique structure to selectively excite fluorophores in specific volumes around the metal. Fluorescence quenching occurs if the excited fluorophore decays through non-radiative channels. There are a variety of forms of quenching, but metal quenching may occur if k_m is larger than the other radiative decay rates.[15]

2.3.2 Fluorescence Correlation Spectroscopy

Fluorescence correlation spectroscopy (FCS) is a statistical tool used to observe fluorescence fluctuations.[7] In an experiment apparatus that utilizes FCS, optical intensities are monitored in a volume (Fig. 4) at a real-time t and at a later time τ (intensities at multiple values of τ are usually recorded). The later time τ is not to be confused with the lifetimes, τ_f and τ_T. The dimensions of the observation volume and the number of unique later time τ recordings depend on the equipment one is using.

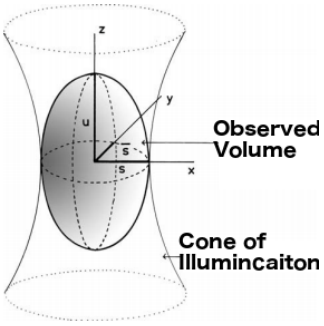

Figure 4: **FCS Observation Volume**

The average number of fluorophores within this volume depends on the concentration of the sample under investigation and this average will remain constant in stationary experiment.[15] Due to the diffusion of the particles in the sample under investigation the intensity observed due to the emissions from fluorophores within the volume at an exact point in time will lead to different intensities being recorded at times t and τ.

The time-dependent intensity changes are analyzed statistically. The intensities $F(t)$ and $F(t+\tau)$, at a time t and τ seconds after t, respectively, are recorded

and compared. When the fluorophores diffuse rapidly the intensity at time t is less likely to match the intensity τ seconds later. When the fluorophores diffuse very slowly, the intensity at a time t is more likely to match the intensity τ seconds later ($F(t) \approx F(t+\tau)$). The two previous statements also depend on the magnitude of τ among other constraints. The FCS instrument will then calculate and produce the autocorrelation function $G(t)$ from the correlation between $F(t)$ and $F(t+\tau)$ for a range of delay times τ. The average number of molecules being observed in an FCS instrument is the amplitude of $G(t)$ for $\tau = 0$. Due to the diffusion of particles in an FCS experiment the fluorophores in the sample are less susceptible to photobleaching. A microscope utilizing FCS has the ability to provide results for the number of observed particles, the diffusion rates along with other dynamic processes. Given an intensity function $F(t)$ at any time t which has an average intensity $\langle F \rangle$, the autocorrelation function for the fluorescence intensities, normalized by the average intensity squared, is

$$G'(\tau) = \frac{F(t)F(t+\tau)}{\langle F \rangle \langle F \rangle} \tag{9}$$

The autocorrelation function of fluorescence fluctuations can then be written as

$$G(\tau) = \frac{\langle \delta F(0) \delta F(\tau) \rangle}{\langle \delta F \rangle^2} \tag{10a}$$

$$G(\tau) = G'(\tau) - 1 \tag{10b}$$

An instrument with a collection efficiency function CEF(r) exposed to an excitation intensity $I(r)$ will produce a detection profile

$$p(r) = CEF(r)I(r) = MDE(r) \tag{11}$$

Where MDE is the molecular detection efficiency. If the FCS system has a quantum efficiency for detection of emitted photons q_f, cross-section of absorption σ_{abs}, and fluorophore quantum efficiency of emission Q then the system will have a brightness $B = q_f \sigma_{abs} Q$. Using $C(r,t)$ as the distribution of fluorophores, where r is actually a vector and the observation volume would be an elliptical volume as in Fig. 4, the

autocorrelation function can also be described by

$$G(\tau) = \frac{B^2 \iint p(r)p(r')\langle \delta C(r,0)\delta C(r',\tau)\rangle dV\, d'V}{[BC \int p(r)dV]^2} \tag{12}$$

Where r is the position of the fluorophore at time $t = 0$ and r' is the position at a later time $t = \tau$.

2.4 Finite-Difference Time-Domain

The finite-difference time-domain (FDTD) method is an approximation method to solve Maxwell's equations. In 1966, Kane Yee introduced the FDTD solution on a computational grid with step divisions in space and time (Fig. 5).[27] Yee's FDTD method takes the finite differences on this computational grid as approximations to the spatial and temporal derivates found in Maxwell's equations.[2] Using a Taylor series expansion, a 1-D function $f(x)$ has a difference-approximation given by[24]

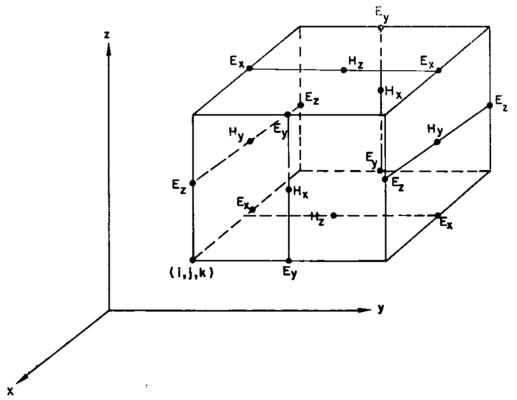

Figure 5: **FDTD Grid**. Rectangular representation of the electronic and magnetic field components

$$\frac{df(x)}{dx}|_{x=x_0} \approx \frac{f(x_0 + \frac{\delta}{2}) - f(x_0 - \frac{\delta}{2})}{\delta} \tag{13}$$

Yee denoted a grid point at $(i, j, k) = (i\Delta x, j\Delta y, k\Delta z)$ and claimed that any function of space and time may be represented as

$$F(i\Delta x, j\Delta y, k\Delta z, n\Delta t) = F^n(i, j, k) \tag{14}$$

Faraday's Law (Eq 1c) and the Ampère-Maxwell Law (Eq 1d) are equivalent to the

[2]The Ampère-Maxwell Law found in Eq 1d is written as $\frac{\partial \boldsymbol{D}}{\partial t} - \boldsymbol{\nabla} \times \boldsymbol{H} = \boldsymbol{J}$ in Yee's paper. The equations solved in this section have modified Yee's solutions so that the work is in agreement with Eq 1d.

following scalar equations in a rectangular coordinate system

$$-\frac{\partial B_x}{\partial t} = \frac{\partial E_z}{\partial y} - \frac{\partial E_y}{\partial z}, \tag{15a}$$

$$-\frac{\partial B_y}{\partial t} = \frac{\partial E_x}{\partial z} - \frac{\partial E_z}{\partial x}, \tag{15b}$$

$$-\frac{\partial B_z}{\partial t} = \frac{\partial E_y}{\partial x} - \frac{\partial E_x}{\partial y}, \tag{15c}$$

$$\frac{\partial D_x}{\partial t} + J_x = \frac{\partial H_z}{\partial y} - \frac{\partial H_y}{\partial z}, \tag{15d}$$

$$\frac{\partial D_y}{\partial t} + J_y = \frac{\partial H_x}{\partial z} - \frac{\partial H_z}{\partial x}, \tag{15e}$$

$$\frac{\partial D_z}{\partial t} + J_z = \frac{\partial H_y}{\partial x} - \frac{\partial H_x}{\partial y} \tag{15f}$$

Equation 16 is the finite difference equation of Eq 15a. The finite difference equations for Eq 15b and Eq 15c are constructed similarly to Eq. 16. Equation 17 is the finite difference equation for Eq 15d. The finite difference equations for Eq 15e and Eq 15f are constructed as has Eq 17.

$$\begin{aligned}\frac{B_x^{n+1/2}(i,j+\frac{1}{2},k+\frac{1}{2}) - B_x^{n-1/2}(i,j-\frac{1}{2},k-\frac{1}{2})}{\Delta t} = \\ \frac{E_y^n(i,j+\frac{1}{2},k+1) - E_y^n(i,j+\frac{1}{2},k)}{\Delta z} - \\ \frac{E_z^n(i,j+1,k+\frac{1}{2}) - E_z^n(i,j,k+\frac{1}{2})}{\Delta y}\end{aligned} \tag{16}$$

$$\begin{aligned}\frac{D_x^n(i+\frac{1}{2},j,k) - D_x^{n-1}(i+\frac{1}{2},j,k)}{\Delta t} + J_x^{n-\frac{1}{2}}(i+\frac{1}{2},j,k) = \\ \frac{H_z^{n-\frac{1}{2}}(i+\frac{1}{2},j+\frac{1}{2},k) - H_z^{n-\frac{1}{2}}(i+\frac{1}{2},j-\frac{1}{2},k)}{\Delta y} - \\ \frac{H_y^{n-\frac{1}{2}}(i+\frac{1}{2},j,k+\frac{1}{2}) - H_y^{n-\frac{1}{2}}(i+\frac{1}{2},j,k-\frac{1}{2})}{\Delta z}\end{aligned} \tag{17}$$

The linear dimensions of the grid must be a fraction of the wavelength, so that the electromagnetic field changes are not significant across one increment in the grid. Assuming $\Delta x = \Delta y = \Delta z$ and constants for the relative permittivity and relative

permeability, ε and μ, respectively, one comes to a stability criterion

$$\sqrt{(\Delta x)^2 + (\Delta y)^2 + (\Delta z)^2} > c\Delta t = \sqrt{\frac{1}{\varepsilon\mu}}\Delta t \tag{18}$$

It has been mentioned that plasmonic surface modes are present for TM polarizations only. Assuming ε and μ are constants, $J = 0$ and that the field components are independent of the z coordinate of a point we arrive at the following equations

$$E_x = 0, E_y = 0, H_z = 0, \tag{19a}$$

$$\varepsilon\frac{\partial E_z}{\partial t} = \frac{\partial H_y}{\partial x} - \frac{\partial H_x}{\partial y}, \tag{19b}$$

$$\mu\frac{\partial H_x}{\partial t} = -\frac{\partial E_z}{\partial y}, \tag{19c}$$

$$\mu\frac{\partial H_y}{\partial t} = \frac{\partial E_z}{\partial x} \tag{19d}$$

Using a distance $\ddot{\delta} = ct = \sqrt{\frac{1}{\mu\varepsilon}}t$ and an impedance $Z = \sqrt{\frac{\mu}{\varepsilon}} = 376.7\Omega$ the finite difference equations for TM waves may be calculated after n time cycles using the following equations

$$\begin{aligned} E_z^{n+1}(i,j) &= E_z^n(i,j) \\ +Z\frac{\Delta\ddot{\delta}}{\Delta x}&[H_y^{n+\frac{1}{2}}(i+\frac{1}{2},j) - H_y^{n+\frac{1}{2}}(i-\frac{1}{2},j)] \\ -Z\frac{\Delta\ddot{\delta}}{\Delta y}&[H_x^{n+\frac{1}{2}}(i,j+\frac{1}{2}) - H_y^{n+\frac{1}{2}}(i,j-\frac{1}{2})], \end{aligned} \tag{20a}$$

$$\begin{aligned} H_x^{n+\frac{1}{2}}(i,j+\frac{1}{2}) &= H_x^{n-\frac{1}{2}}(i,j+\frac{1}{2}) \\ -\frac{1}{Z}\frac{\Delta\ddot{\delta}}{\Delta y}&[E_z^n(i,j+1) - E_z^n(i,j)], \end{aligned} \tag{20b}$$

$$\begin{aligned} H_y^{n+\frac{1}{2}}(i+\frac{1}{2},j) &= H_y^{n-\frac{1}{2}}(i+\frac{1}{2},j) \\ +\frac{1}{Z}\frac{\Delta\ddot{\delta}}{\Delta x}&[E_z^n(i+1,j) - E_z^n(i,j)] \end{aligned} \tag{20c}$$

3 Methods

Optical properties of materials used in our calculations are obtained from previous experimental measurements (i.e. those of Johnson and Christy or Palik and Ghosh).[8][10][21] The materials are chosen for fabrication using the facilities at the University of California in Santa Cruz. Simulations were first performed to benchmark our work to previously documented results to verify our usage and understanding of the software package and also the physical phenomena. Benchmarking included: (*i*) FDTD simulations to calculate cross-sections, (*ii*) analytical computations to compare material fit and (*iii*) FDTD simulations to verify enhancements.

3.1 Material Properties: Cross-Sections

Before simulating the surface enhanced excitation and emission of fluorophores in presence of metallic surfaces, we first benchmarked plasmonic properties of metals. These metallic nanoparticles exhibit different behavior depending on the chemical element, the size and shape of the metal, the energy and polarization of the incident electromagnetic radiation as well as the angle of incidence (the surrounding medium affects the angle of incidence due to Snell's law).

3.1.1 Analytical Cross-Sections

Cross-section simulations will provide an understanding of plasmonic behaviors and aid in choosing the metal type and dimensions for our custom design. We compared our Ag and Au simulation results to those presented by Klar, which were calculated Mie theory curves and also to the Al simulation results of Chowdhury et al.[3][12] The optical cross-section equations for a spherical nanoparticle are

$$\sigma_{sca} = \frac{3}{2\pi}(\frac{\omega}{c})^4 \varepsilon_{diel}^2 V^2 \frac{(\varepsilon'_{met} - \varepsilon_{diel})^2 + (\varepsilon''_{met})^2}{(\varepsilon'_{met} + 2\varepsilon_{diel})^2 + (\varepsilon''_{met})^2}, \tag{21a}$$

$$\sigma_{ext} = 9\frac{\omega}{c}{\varepsilon_{diel}}^{3/2} V \frac{\varepsilon''_{met}}{(\varepsilon'_{met} + 2\varepsilon_{diel})^2 + (\varepsilon''_{met})^2}, \tag{21b}$$

$$\sigma_{abs} = \sigma_{ext} - \sigma_{sca} \tag{21c}$$

Where the dielectric constant $\varepsilon_{met} = \varepsilon'_{met} + i\varepsilon''_{met}$ is for the metal and the dielectric constant of the surrounding medium ε_{diel} is purely real.[12] In order to compute the cross-section efficiency for absorption Q_{abs} the cross-section σ_{abs} is divided by the geometric cross-section πr^2 (the area of a 2-dimensional slice that cuts through the center of the nanoparticle).[3][14]

$$Q_{abs} = \frac{\sigma_{abs}}{\pi r^2} \tag{22}$$

3.1.2 FDTD Simulation Method

A total-field scattered-field (TFSF) source is a source model employed in our FDTD simulations that conveniently isolates the scattered fields of a simulation from the incident field. Upon placing a nanoparticle at the origin of our simulation, the point of incidence of the TFSF source was placed on the x axis a distance x' from the origin. The metal has a radius r such that $|x'| \approx 3r$. The TFSF source is set to propagate along the x direction towards the metal and contain the incident source in a cube with sides of length $2x'$. The angle of incidence of the TFSF source must be set normal to the surface of the metal. Also, to determine cross-sections we set our FDTD simulation with a mesh step size of $\ddot{\delta} \approx 5\lambda \times 10^{-4}$, cubic mesh span with sides $> 2x'$, a total simulation region in the shape of a cube with minimum length 1.5λ, a minimum of 10 PML layers[3], a simulation time $dt = 350$fs and a background index of 1.33 (the index of refraction of water).

3.1.3 Ag and Au Cross-Section Results

Cross-section simulation results of TFSF source power P_0 and intensity I_0 are then recorded. The absorption cross-section σ_{abs} is determined by recording the unit-less fraction of power transmitted T_{abs} into a monitored absorption volume $V_{abs} < V_0$. The scattering cross-section σ_{sca} is produced from the fraction of power transmitted T_{sca} out of a volume V_{sca} (with $V_{sca} > V_0$). The volumes V_0, V_{sca}, and V_{abs} all share

[3]Perfectly Matched Layers (PMLs) at the boundaries allow for smaller simulation spans and produce solutions faster. Depending on the simulation settings one may change the boundary settings to symmetric, anti-symmetric or periodic as well. Periodic PML layers are useful when simulating periodic structures in order to observe SPPs effects

the same origin.

$$\sigma_{abs} = -T_{abs} P_0 / I_0 \tag{23a}$$

$$\sigma_{sca} = T_{sca} P_0 / I_0 \tag{23b}$$

The extinction cross-section was calculated using Eq. 21c. The ratio of power (units, W) to intensity (units, W/m^2) produces units of area (m^2).

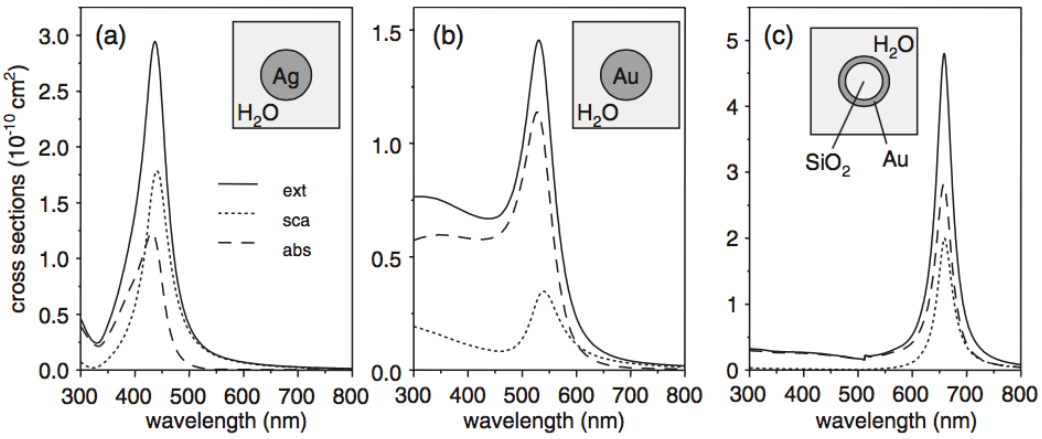

Figure 6: **Published Cross-Section Results**. Nanoparticle cross-sections published results for Ag sphere, Au sphere and Au shell

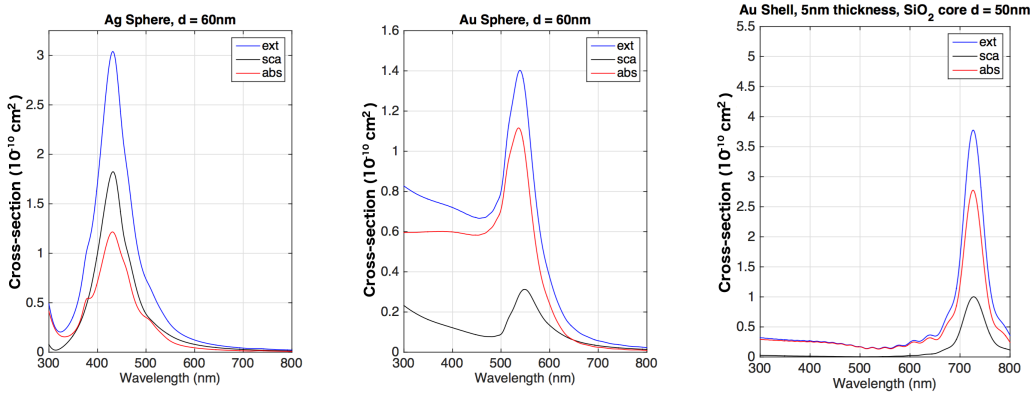

(a) (b) (c)

Figure 7: **Ag and Au Nanodevice Simulation Cross-Section Results**. Simulation results for cross-sections of (a) 60m diameter Ag sphere, (b) 60nm diameter Au sphere, (c) 50nm diameter SiO_2 core surrounded by 5nm thick Au shell.

The results for Ag (Fig. 7a) match very closely to published results (Fig. 6), the largest discrepancy occurred in the Au particle simulations (Fig. 7b,c).[12] Figure

7 demonstrates that the extinction cross-section σ_{ext} of a solid Ag nanoparticle is twice that of a solid Au nanoparticle of the same shape and size. Not only is σ_{ext} of Ag greater than that of Au, but for values of $\lambda < 340$nm and $\lambda > 540$nm, σ_{ext} of Ag is an order of magnitude less than that at the Ag maximum σ_{ext} value. The magnitude of the Au particle σ_{ext} is roughly half of the maximum of the Au σ_{ext} for λ 100nm less than the peak wavelength ($\lambda_o \approx 540$nm). The Au shell has the largest σ_{ext} and narrowest peak ($\Delta\lambda$ for Au is smallest) of these three simulations. The Ag solid and Au shell are reminiscent of narrow passband filters. Whereas the Au sphere resembles a high-pass filter that has gain at the lowest passed frequencies (high pass meaning it passes high frequencies, or low wavelengths).

3.1.4 Al Cross-Section Results

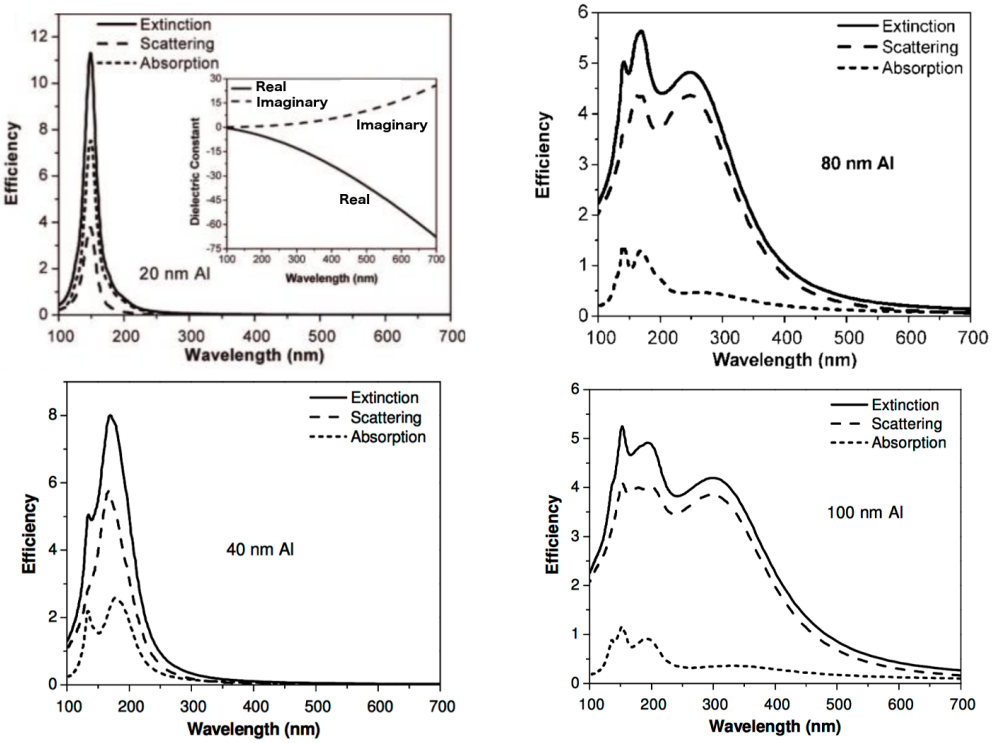

Figure 8: **Al Cross-Sections from Literature**. Cross-section curves for Al particles of diameters 20-, 40-, 80- and 100-nm.[3]

Aluminum is a metal that is commonly used in ZMW devices. Al nanoparticle cross-sections are calculated and benchmarked with analytical calculations. Our FDTD calculations (Fig. 9) match closely with the published calculations (Fig. 8)

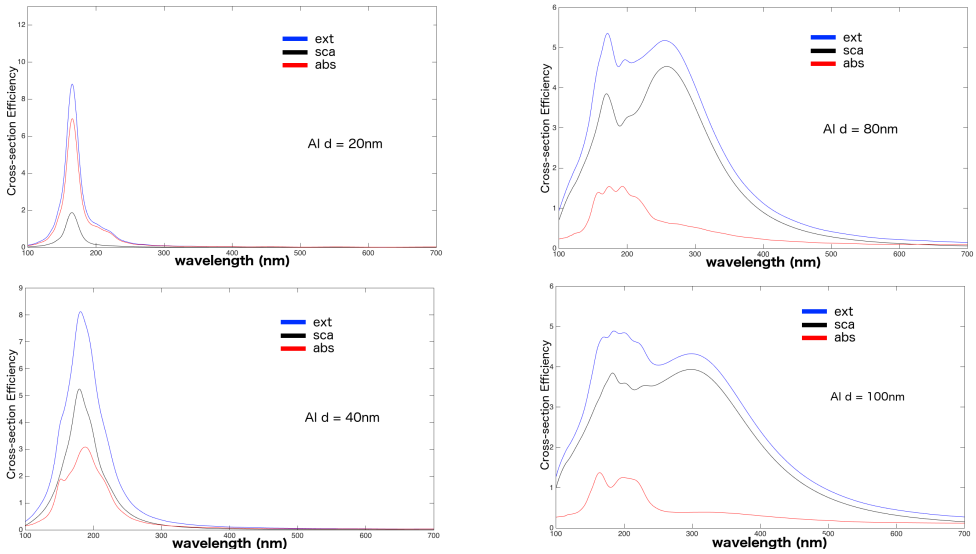

Figure 9: **Al Cross-Sections from Simulations** FDTD simulation results of Al cross-sections of 20-, 40-, 80- and 100-nm diameter.

of Chowdhury, et al.[3] Figures 8 and 9 clearly show that as the particle dimensions decrease the peak cross-section magnitude increases and the $\Delta\lambda$ about the peak decreases (analogous to the Q-factor of a resonator circuit). The plots for the Al nanoparticles of larger diameter demonstrate the presence of higher order modes (the multiple peaks).[3]

3.2 Material Properties: Dielectric Function

An investigation on the optical response of metals for a variety of published experimental results is presented here. A material fit for our FDTD simulations based upon these published results is also documented. Figure 10 depicts the effects of modifying the dielectric function $\varepsilon(\omega)$ published results of Palik and Ghosh for an Al nanoparticle to produce different material fits. The material fit of Al is here modified by adjusting the desired wavelength range (λ_{min} and λ_{max}) and also the simulation time dt.

3.2.1 Analytical Calculation of Fluorescence Enhancement

Analytical calculations were then investigated using published raw experimental data for the dielectric function $\varepsilon(\omega)$ of Au and Ag. Analytical results were also obtained

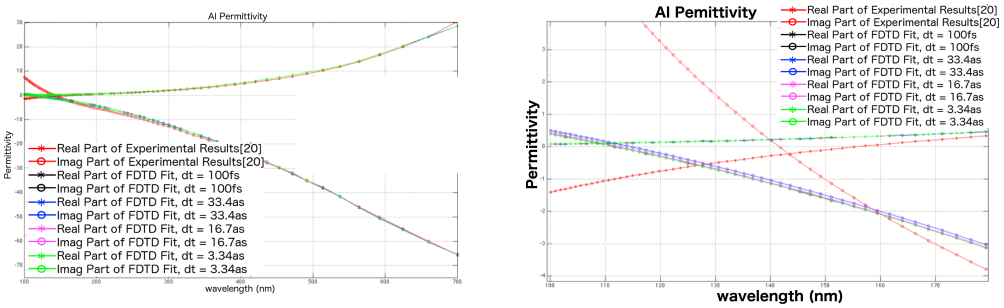

(a) (b)

Figure 10: **Dielectric Function of Al**. Dielectric function from Palik and Ghosh raw experimental results of aluminum $\varepsilon(\omega)$ and different software fits

from FDTD software fits of the dielectric functions. The raw and fit dielectric functions ε for Ag and Au were exported from the FDTD simulation software to calculate the fluorescence enhancement. Figure 11 was generated using equations published in Bharadwaj and Novotny.[1]

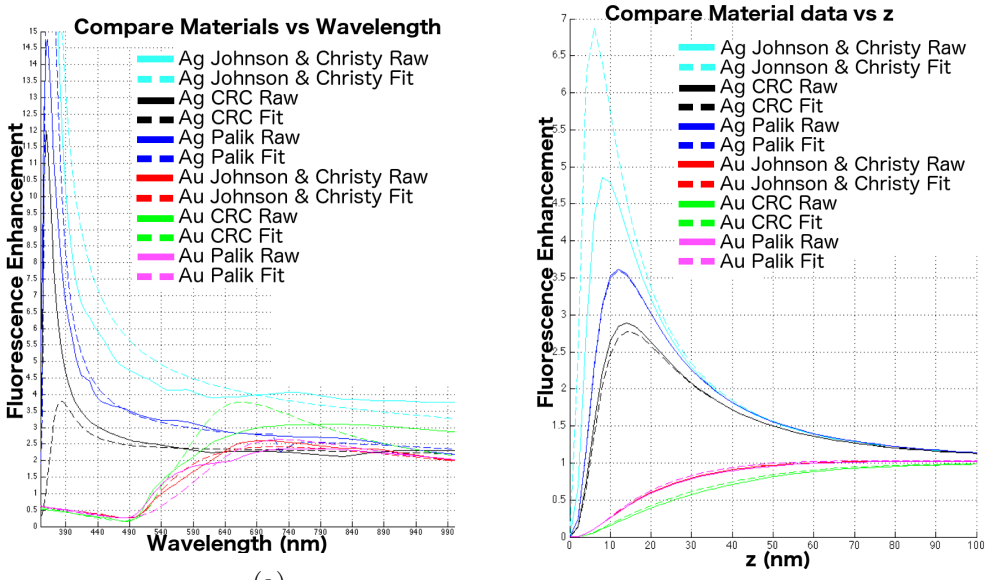

(a) (b)

Figure 11: **Fluorescence Enhancement Material Fit Comparison**. Analytical results comparison from material experimental data and the fit of this data used in the simulation for Ag and Au nanoparticles versus (a) wavelength λ and (b) depth s along z with $\lambda = 488$nm.

3.2.2 Results of Analytical Fluorescence Enhancement

The main observations are the differences which arise from the variations of the relative permittivity from different experimental results for the same material. The Ag nanoparticle has a larger fluorescence enhancement (≈ 6.8), the Au nanoparticle displays a flat response for distances greater than 40nm at $\lambda = 488$nm. Meaning that a fluorophore lying 40nm to 100nm away from the Au nanoparticle will be enhanced by the same amount, this is akin to having a flat spatial response.

3.3 Fluorescence Enhancement Simulation Method

To obtain fluorescence enhancement results from simulations a fluorophore was modeled as a dipole source radiating at the fluorophore emission wavelength. The power from the dipole source in the simulation is recorded as P_F. When the dipole is radiating in an inhomogeneous medium the dipole radiation is a fraction of the total source power P_S. The fraction of power transmitted by the dipole in the simulations is stored as fluorophore radiative decay rate Γ. The non-radiative decay rate k_{nr} is obtained by subtracting the radiative decay rate Γ from the normalized dipole power P_F/P_S.

Once the internal fluorophore results were recorded, a metallic structure was introduced and MEF simulation results were collected for power P_T, radiative emission rate Γ_T and non-radiative decay rate k_T . From these results we could now calculate the fluorescence enhancement (Γ_T/Γ) of the MEF structure. The quantum yields of the isolated fluorophore Q_f and that of the MEF Q_T may be obtained using the radiative emissions rate Γ and Γ_T, respectively, and the corresponding lifetime (τ and τ_T).

3.3.1 Fluorescence Enhancement of Monomers and Dimers

Before enhancement factor calculations of waveguide structures, we performed simulations of simple nanoparticles. Simulations for two distinct structure formations were benchmarked using a silver monomer: (i) a dipole source placed a distance s from and oriented normal to the surface of the monomer of diameter d (Fig. 12

and inset of Fig. 13a) or (*ii*) the dipole source a distance s from and in a parallel orientation to the surface of the nanoparticle with diameter d. Experiments were carried out for various values of s and d.

Dimer simulations were conducted in an identical manner to those of the monomer. The exception here is that there is a second nanoparticle placed a distance $2s$ from the first nanoparticle. The dipole is placed at the midpoint between the two nanoparticles.

The two nanoparticles in the dimer simulations each have a diameter d and are of the same material type, Ag. The dimer system is examined for various values of s and d. Dimer simulations are also performed for parallel or perpendicular (inset of Fig. 13b) dipole orientations.

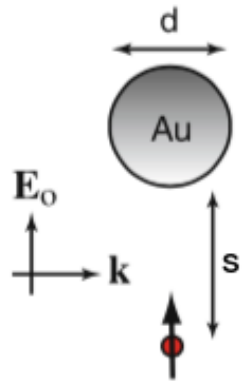

Figure 12: **Au and Perpendicular dipole**

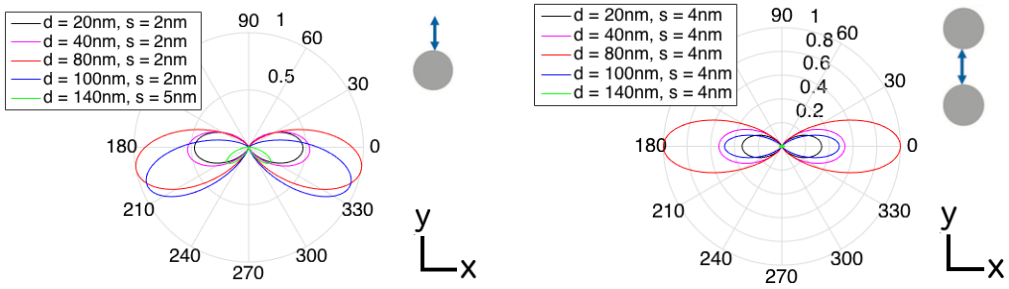

Figure 13: **Far-Field Radiation Patterns**. Radiation patterns for a fluorophore modeled as a dipole in perpendicular orientation to the surface of (a) a Ag monomer system and (b) a Ag dimer system

Simulations were administered to calculate: the far-field radiation pattern (Fig. 13), near-field intensity distribution and the two dimensional emission enhancement patterns. The near-field intensity distribution I_{nf} in arbitrary units displayed in Fig. 14a is determined by taking the logarithm of the dimer system power P_T normalized

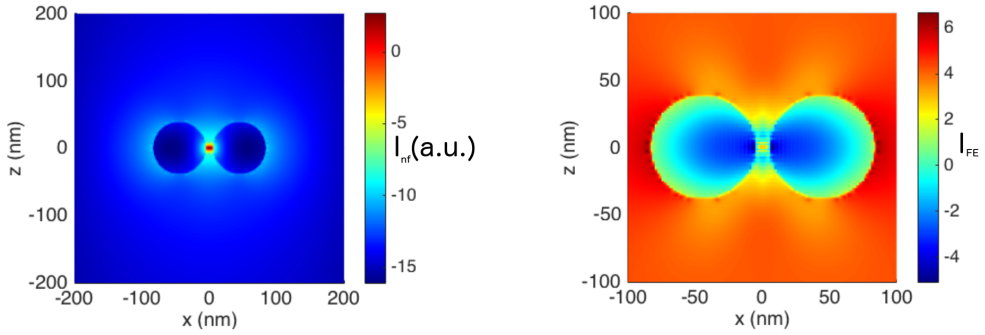

(a) (b)

Figure 14: **Dimer Intensity Patterns**. The (a) near-field intensity I_{nf} and (b) emission enhancement patterns I_{FE} of an 80nm diameter Ag dimer system spaced 10nm apart surface-to-surface with a fluorophore placed at the midpoint between the two particles and oriented with a normal to the two surfaces.

by the maximum power of the fluorophore $P_{F,max}$

$$I_{nf}(x,y) = \log_{10} \frac{P_T(x,y)}{P_{F,max}} \tag{24a}$$

$$I_{FE}(x,y) = \log_{10} \frac{P_T(x,y)}{P_F(x,y)} \tag{24b}$$

The two-dimensional emission enhancement pattern I_{FE} in Fig. 14b is generated by taking the logarithm of the dimer-system power $P_T(x,y)$ by the two-dimensional output power of the single fluorophore $P_F(x,y)$. Depending on the polarization of the fluorophore in respect to that of the surrounding structure the resulting intensity patterns are oriented in different directions and have different enhancement factors.

3.4 Waveguide Comparison

In this section, simulations were investigated to compare and contrast three different etch designs from literature in structures composed of a thin film of metal or in a stack of thin metal films. Simulation for the response of the system to changes of source wavelength, location, polarization and type was determined. The three apertures we studied were: *(i)* conventional waveguides, *(ii)* waveguides with a bowtie etch and *(iii)* rectangular etch patterns in a waveguide; also, these patterns were etched into single metal films on glass substrate and *(iv)* into a metal-stack waveguide (heterogeneous structure). We then combined the results of these simulations

with the theoretical investigations to create a novel design (Fig. 27).

3.4.1 ZMW Enhancement Simulation Method

The results to determine excitation source confinement and enhancement are produced by simulating the waveguide structure with a circularly polarized excitation source propagating normal to the glass-metal interface (along the z-axis). The origin of the simulation excitation source is within the glass substrate and propagates towards the thin metal film. The dipole source was only used in simulations for the conventional ZMW to benchmark with published results. Figure 15 visually describes the normalized near-field intensity I_{nf} produced by a dipole source of different polarizations found 50nm from the glass substrate and at the center of the circular etch.

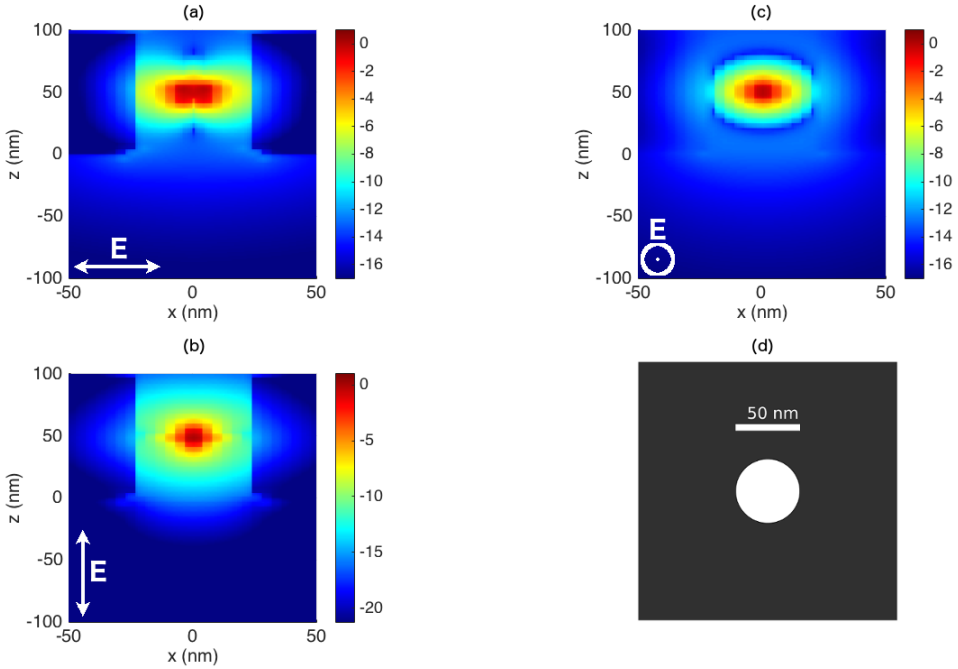

Figure 15: **Near-Field Intensity of Conventional ZMW**. Figures of the near-field intensity of a conventional ZMW in the xz-plane with a fluorophore oriented along the (a) x, (b) z and along (c) y axes; (d) is an illustration of the cylindrical etch viewed in the xy-plane.

There were four simulations performed to collect data for source confinement. The source only simulations were performed without a structure and only: *(i)* a linearly polarized source polarized along the x-axis and *(ii)* a linearly polarized source with

polarization 90° and phase 90° to that of the previous simulation, along the y-axis. The two linearly polarized source only results were combined to represent the circularly polarized source. The structure was then introduced and two simulations were run again to collect the confinement results for x and y source polarizations.

3.4.2 Circular Mask

Investigations of the optical confinement and emission enhancement produced by a zero-mode waveguide composed of a circular etch (conventional ZMW) of 50nm diameter into a 100nm thick Al film are presented here. The simulation results of excitation source confinement of a conventional zero-mode waveguide are found in Figure 16. For simulation purposes, the excitation source was placed in the glass substrate and 300nm before the glass-metal interface which are represented by the lines in Figure 16b.

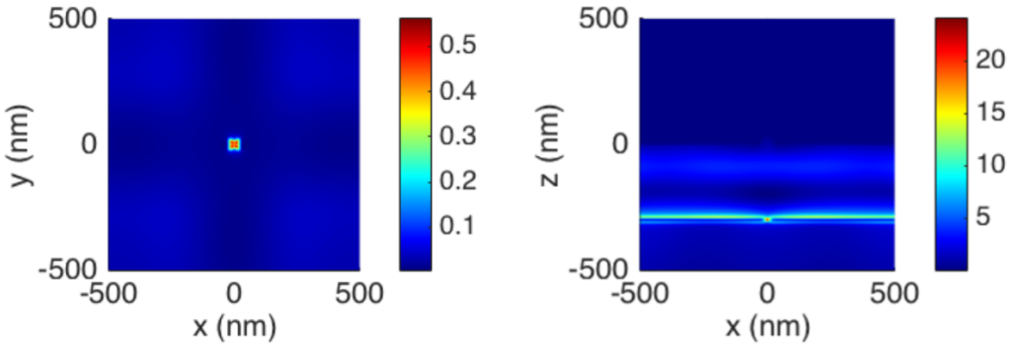

(a) (b)

Figure 16: **Excitation Source Confinement and Enhancement of Conventional ZMW**. Circularly polarized light source confinement in the (a) xy- and (b) xz-planes; note the plane wave patterns at z = -300nm, this is where the simulation excitation sources are located.

3.4.3 Bowtie Mask

A bowtie aperture of base length 450nm was then investigated for optical confinement (Fig. 17). The bowtie mask consists of two right isosceles triangles each of base length 450nm joined at their respective right angles. The sides of these triangles are 318.2nm long. A square mask of side length 30nm shares it's center with the vertices of the right angles of the two isosceles triangles. This mask was etched

into a 170nm thick film of Al and simulated.

Figure 17: **Bowtie Mask**

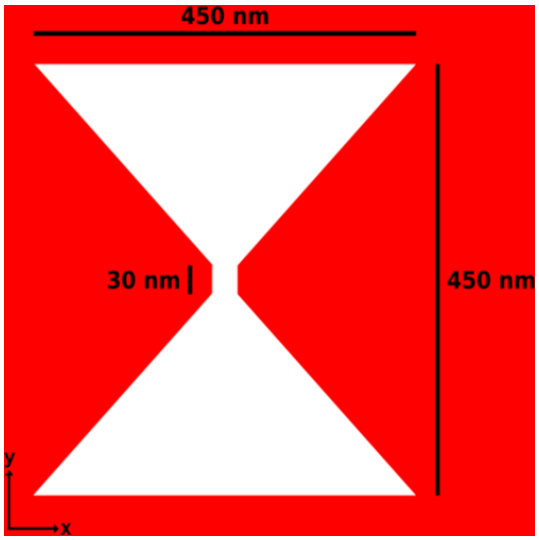

The maximum intensity from the optical confinement along the xy-plane of a bowtie aperture is greater than that of the conventional ZMW (Fig. 18a). The xy-plane light is primarily found near the square mask portion of the bowtie aperture, however, one can see a spread of source light into the two isosceles triangle mask areas. The excitation source confinement along the xz-plane demonstrates the focusing of light into a small range in x but the light is found throughout the entire thickness (and slightly beyond) of the thin film.

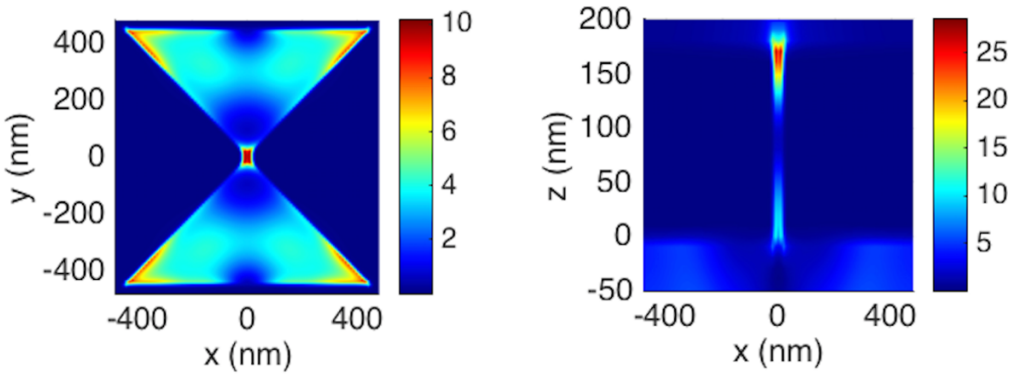

(a) (b)

Figure 18: **Excitation Source Confinement and Enhancement of Bowtie Aperture**. The excitation source confinement along the (b) xy-plane and (c) xz-plane.

A ZMW with a bowtie etch will have distinct results depending on the the polarization of the incident light source. A smaller confinement volume will be generated when an excitation light source propagating from the glass substrate to the normal of the glass-metal interface (z) and linearly polarized along x (Fig. 19a) than when the source is polarized perpendicularly along y (Fig. 19b). Not only is the confinement volume smaller for polarization in the x-direction but the maximum intensity

in the focused regions is of higher value than that for a similar source polarized in the y-direction.

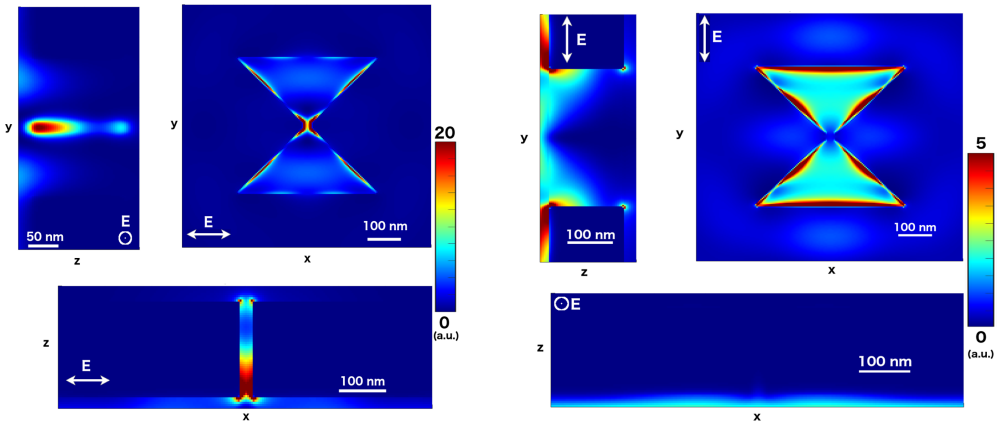

(a) (b)

Figure 19: **Bowtie Aperture Linearly Polarized Source Confinement and Enhancement**. Intensity from 450nm bowtie etch of 170nm thick Al film from (a) a perpendicularly incident light source polarized along x and (b) with the same incident source polarized along y.

3.4.4 Rectangular Mask

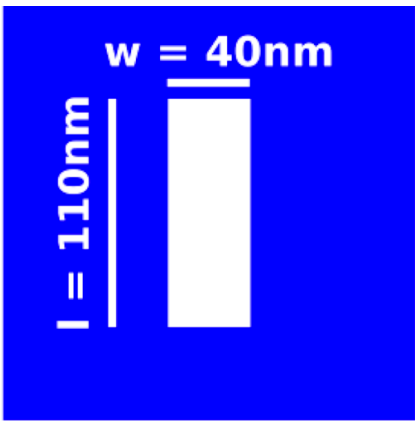

Figure 20: **Rectangular Mask**

The last etch pattern from literature investigated and simulated is the rectangular etch pattern. All rectangular masks investigated were etched into 100nm thick metal films composed of either Al or Au. Figure 20 demonstrates the rectangular mask used for the single film simulations and also the rectangular metal-stack simulations found in the following section. An Al film of 100nm thickness was etched with a rectangular mask of length l = 160nm, width w = 40nm and height h = 100nm. A film of 100nm thick Au was etched with a rectangular mask of dimensions l = 110nm, w = 40nm and h = 100nm.

The results on cross-sections from Section 3.1 demonstrated the optical response of the metals Ag, Au and Al. Simulations for Al nano-shells were not examined so

there is no direct comparison with Au-shells to be found in this text; however, a shell behaves much like a hybridization of elementary modes (Fig. 21).

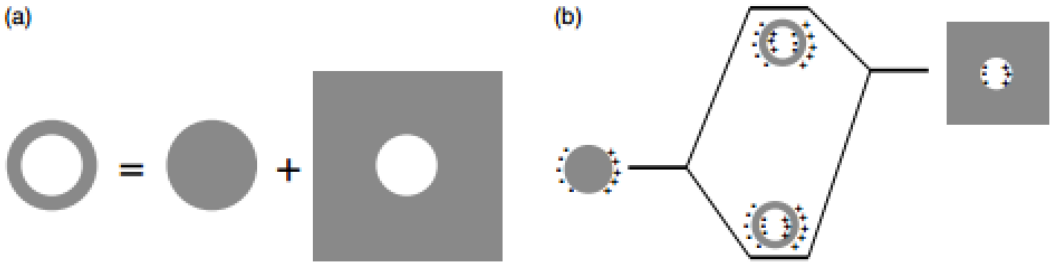

Figure 21: **Hybridization of Elementary Modes**. Graphical representation of complex structures calculated by combing calculations of elementary modes.[20]

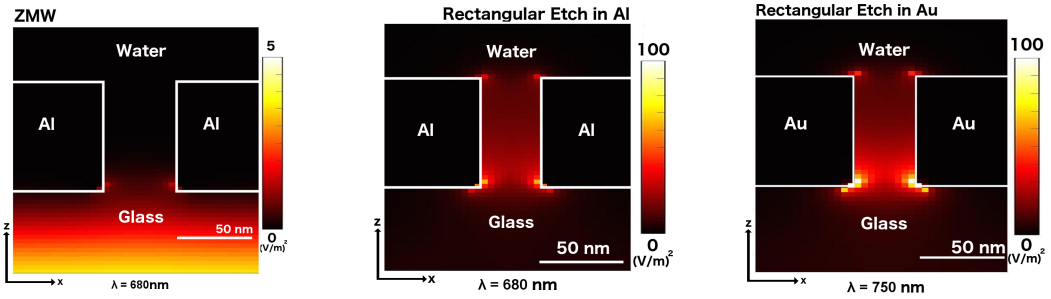

Figure 22: **Confinement and Enhancement of Circular and Rectangular Apertures**. (a) A conventional ZMW of diameter 50nm in 100nm thick Al, (b) 100nm thick Al film etched by a rectangular mask with $l = 160$nm and $w = 40$nm and (c) a rectangular etch in 100nm thick Au film with mask dimensions $l = 110$nm and $w = 40$nm.

The simulations and literature results show that a spherical nanoparticle of Al measuring 40- and 80-nm in diameter have a maximum extinction cross-section efficiency of 8 and 5.75, respectively, at $\lambda \approx 175$nm. The Au nano-sphere of diameter $d = 60$nm produces a maximum extinction cross-section efficiency of 1.33 at $\lambda \approx 550$nm.[4] As mentioned in the cross-section results the Au nano-shell produces a larger cross-section than the Au nano-sphere. The Au nano-shell has a computed extinction cross-section efficiency of 4.4 at $\lambda \approx 660$nm. The Al nano-spheres with $d = 40$- and 80-nm have an extinction cross-section efficiency of 0 and 0.25, respectively, with $\lambda \approx 680$nm. For wavelengths in the the 500- to 700-nm range the cross-section results of Al behave as an optical attenuator. This explains the small optical confinement

[4] $Q_{ext} = 1.5{\times}10^{-10} cm^2/(\pi 60nm^2)$

volumes a conventional ZMW produces for these wavelengths (Fig. 15, 16, 22a). Using a rectangular etch pattern in a 100nm thick Al film produces a larger emission enhancement than that found in a conventional ZMW (Fig. 22b). Using a rectangular etch pattern of similar dimension in a 100nm thick film of Au produced a larger enhancement (Fig. 22c). The rectangular etched films produced a larger emission enhancement but suffered from a larger confinement volume. The Au film also has a greater contrast in intensity throughout the aperture than the intensity contrast found in the Al film with rectangular etch.

3.4.5 Apertures in Metal-Stacks

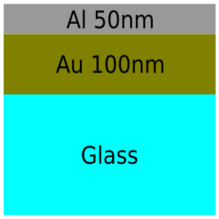

Figure 23: **The Metal-Stack**

This section examines and provides results of ZMWs designed using a stack of two different metal films (Fig. 23). As introduced in the previous section, a metal may behave as an attenuator or amplifier at a wavelength λ depending on the plasmonic characteristics of the metal. Combining the enhancement of Au around 680nm and the attenuation of Al near 680nm a study of rectangle and bowtie masks etched into a metal-stack were undertaken to both confine light and enhance the emissions of light from the volume of confinement. The metal-stack devices consist of a glass substrate placed underneath a stack of Au film of 100nm thickness covered by a 50nm thin film of Al. The metals were then etched with either a rectangular pattern of dimensions w = 40nm, l = 110nm and h = 150nm (Fig. 24-25) or with a bowtie pattern of base length 450nm (Fig. 26). The rectangular etch in a metal-stack ZMW shows improvement over a conventional ZMW (Fig. 16) and bowtie aperture (Fig. 18). The bowtie aperture in a metal-stack shows the largest enhancement and smallest excitation volume of these structures.

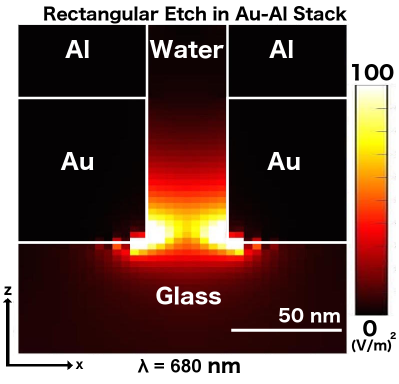

Figure 24: **Rectangle Etch in Metal-Stack**. Confinement and enhancement of a metal-stack ZMW with rectangle etch measuring l = 110nm, w = 40nm and h = 150nm.

Placing the Au nearest to the glass substrate causes there to be a greater enhancement near the glass-metal interface. Since the Al film behaves as an attenuator near $\lambda = 680$nm the light has a smaller confinement volume in the aperture. The bowtie and rectangular etch combined with a metal-stack show promising results. In the following section a novel design will be examined that looks to further enhance and confine light to a smaller volume.

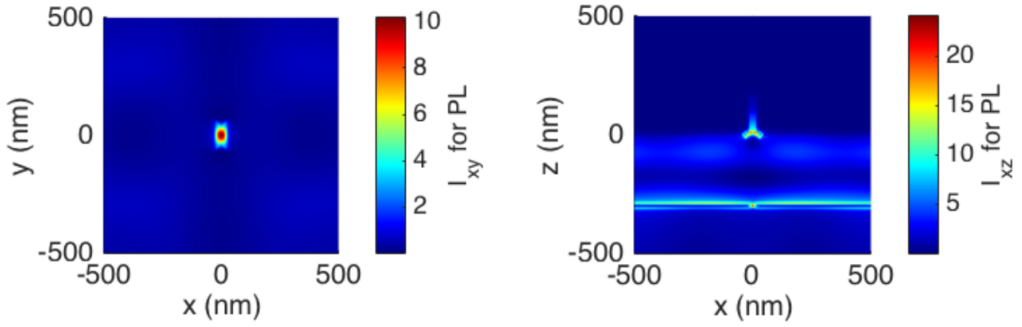

(a) (b)

Figure 25: **Excitation Source Confinement and Enhancement of Metal-Stack with Rectangle Etch**. The confinement and enhancement of a circularly polarized light source along the (a) xy-plane and (b) xz-plane.

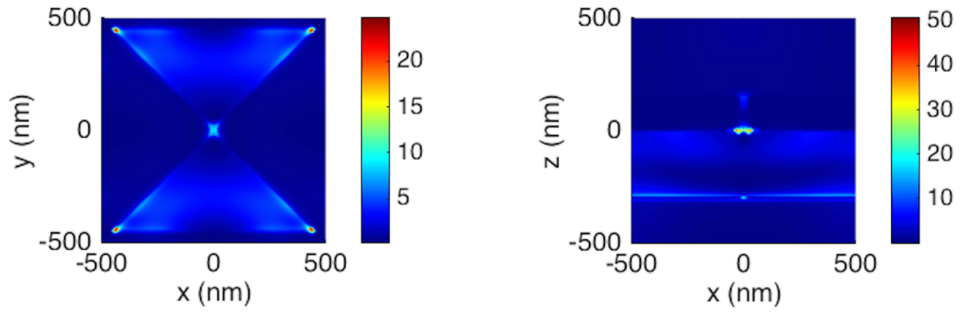

(a) (b)

Figure 26: **Excitation Source Confinement and Enhancement of Metal-Stack with Bowtie Etch**. The confinement and enhancement a metal-stack etched with a 450nm base bowtie pattern excited by a circularly polarized light source along the (a) xy-plane and (b) xz-plane.

4 Novel Design

We merged the confinement produced by multiple stacks of metallic films with the effects of plasmonic near field enhancement for our novel design (Fig. 27).

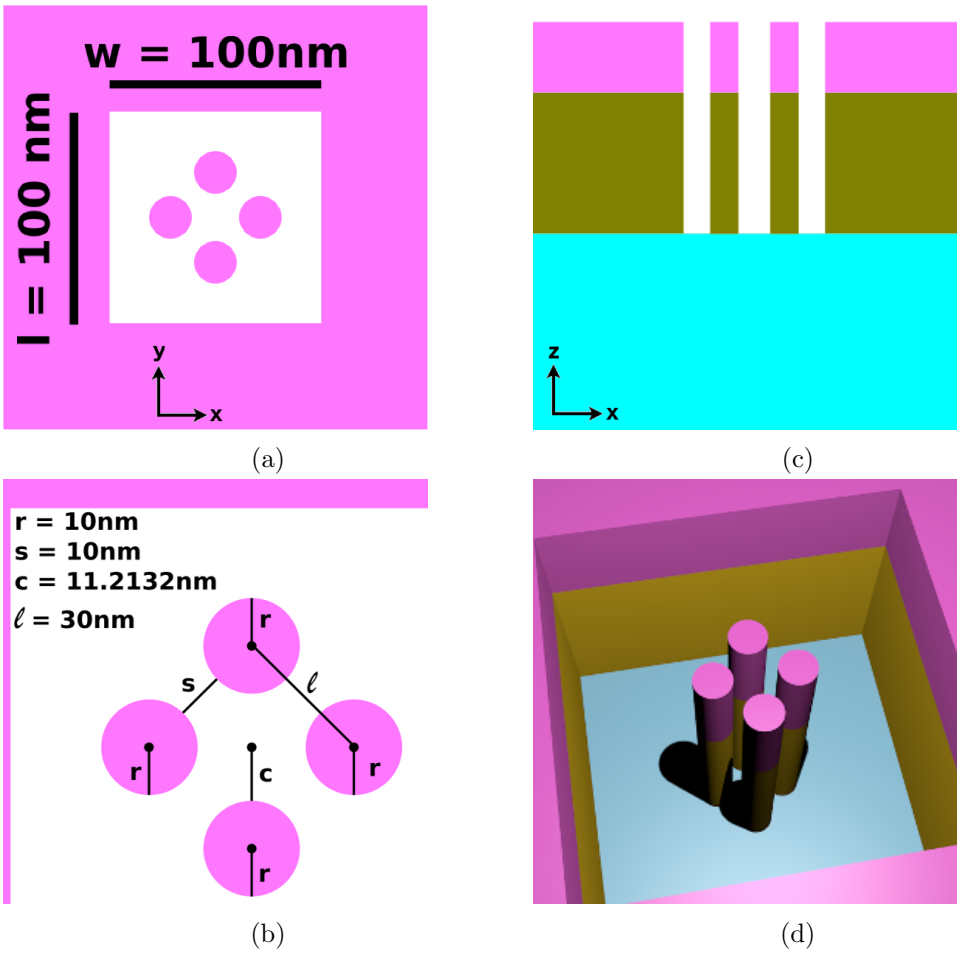

Figure 27: **Rectangular Aperture with Heterogeneous Stack**. Illustrations of a 150nm metal-stack with square etch of sides measuring 100nm with four metal-stack columns not removed by the square etch. The pink material in the illustrations is the 50nm thick Al slab, colored pink to match the curve in Fig. 13. The 100nm thick Au film is the olive tone which sits between the pink Al film and the glass substrate which is in blue. Illustration (a) is a top-down view with etch dimensions, (b) the top-down view with values for spacing and dimension of the columns, (c) side view of the xz-plane at $y = 0$ and (d) a 3-*dimensional* illustration of the structure.

The structure was simulated with a 150nm thick metal-stack (100nm Au film and 50nm Al film) and etched with a square mask of side length 100nm. The structure also includes four metal-stack columns in the aperture space. Each column is designed just as the 150nm metal-stack; a 50nm thick Al column placed above a 100nm thick Au column, with all four columns standing atop the glass substrate. A column radius r of 10nm was selected based on monomer and dimer radiative antenna results. The nearest column to column distance s used in our simulations is 10nm based on the premise that this is the smallest feasible etch resolution. The

center of each column was placed 21.2132nm away from the center of the square aperture; the shortest distance c from the center of the aperture to the surface of a column would then be 11.2132nm.

Our studies and simulations of waveguides using an etched film of Al clearly demonstrated the ability to confine light. Studies and simulations on Ag and Au nanoparticles exhibited the largest emission enhancements of the three metals investigated. The results of our simulations verify that modifying the dimension and pattern — circle, bowtie or rectangle — etched into a thin metal film will result in an enhancement of the radiative decay of a quantum emitter.

4.1 Results

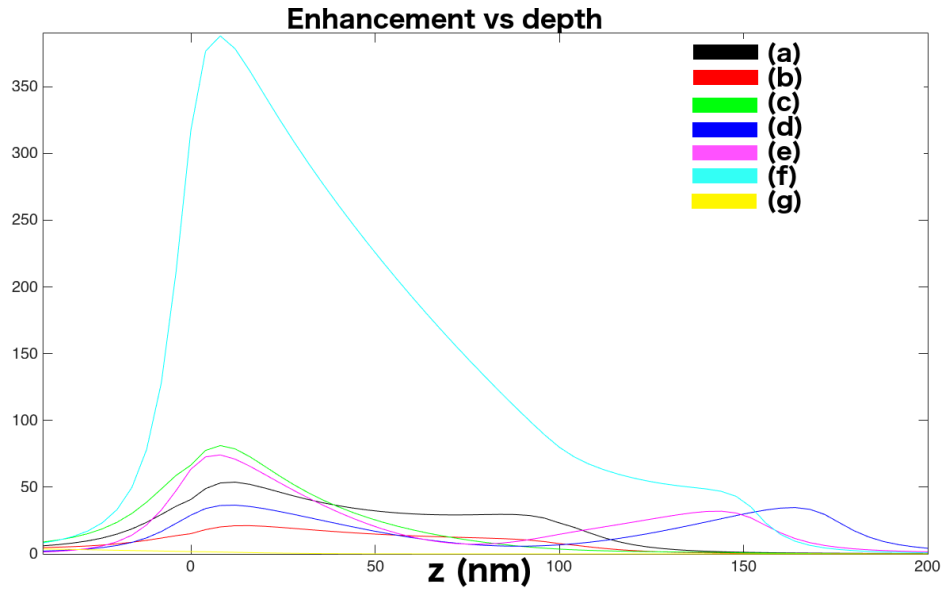

Figure 28: **Depth Dependence of Structure Enhancement**. The enhancement along depth $(0, 0, z)$ from a source of normal incidence to the glass-metal interface polarized along the $x - axis$: (a) Au film with rectangle etch, (b) Al film with rectangle etch, (c) metal-stack with rectangle etch, (d) Al film etched with 150nm bowtie pattern, (e) 170nm metal-stack with 150nm bowtie etch, (f) 150nm metal-stack with rectangle etch and columns in etch and (g) conventional Al ZMW.

For an excitation source with $\lambda = 500$nm and normal incidence to the glass-metal interface (along z) polarized along the direction of maximum enhancement (x) a conventional waveguide produced an enhancement of ≈ 2.[5] Changing λ to 648nm,

[5]For the waveguides in this paper, the polarization direction of maximum enhancement and minimum observation volume for bowtie and rectangle etches is in the x direction and the polarization

a waveguide of Al film with a rectangle etch ($w = 40$nm, $l = 160$nm)produced an enhancement of ≈ 21 at $z = 15$nm. A waveguide of Au film with a rectangle etch of $l = 110$nm produces an enhancement of ≈ 54 at $z = 15$nm and with $\lambda = 688$nm. A waveguide designed of 170nm thick Al etched with a bowtie of hypotenuse length $= 150$nm produces an enhancement of ≈ 36 at $z = 15$nm and $\lambda = 723$nm.

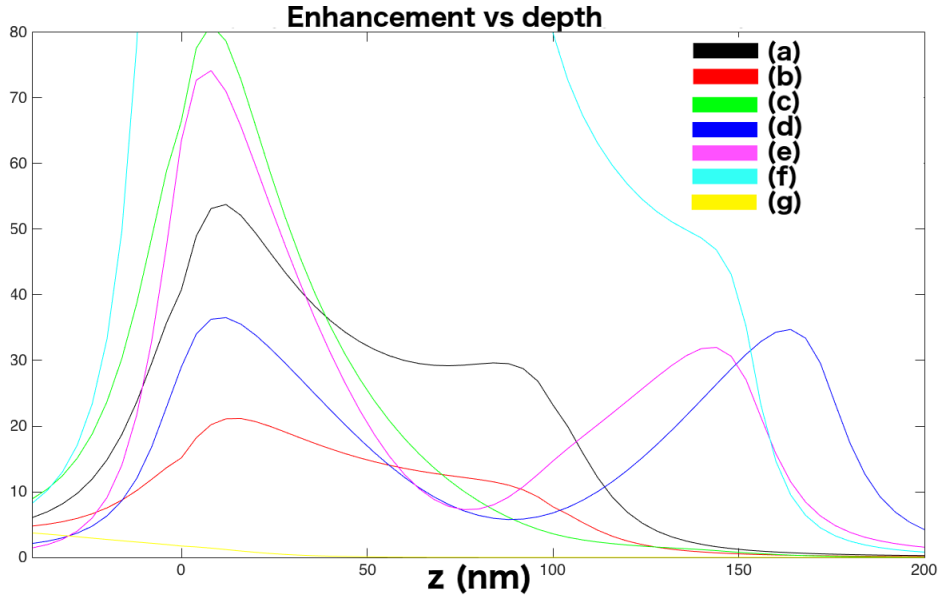

Figure 29: **Zoomed-in Depth Dependence of Structure Enhancement**. The enhancement along depth $(0, 0, z)$ from a source of normal incidence to the glass-metal interface polarized along the $x - axis$: (a) Au film with rectangle etch, (b) Al film with rectangle etch, (c) metal-stack with rectangle etch, (d) Al film etched with 150nm bowtie pattern, (e) 170nm metal-stack with 150nm bowtie etch, (f) 150nm metal-stack with rectangle etch and columns in etch and (g) conventional Al ZMW.

Simulations were run on metal-stacks with rectangular and bowtie etches incorporating the metal columns before arriving at the novel design from Fig. 27. The enhancement factor more than doubles for structures having either bowtie or rectangular etch in a metal-stack of total thickness 150nm versus a single Al film of thickness 100nm. The enhancement factor for a rectangular aperture in a 150nm thick metal-stack is less than double, $\approx 1.5\times$, that of the same structure composed of a single 100nm thick Au film. However, the enhancement of x-polarized light is confined to a smaller volume in the rectangular etch of a metal-stack than that of a

direction of minimum enhancement and larger observation volumes is in the y. For the bowtie, this direction runs parallel to the hypotenuse, or base, of the triangles in the bowtie mask. In the rectangular apertures, the direction is parallel to the width or the narrowest side of the aperture.

single Au film with rectangle etch. A metal-stack etched with a rectangle mask and columns like those in the novel design produced an enhancement of ≈ 400 at a depth $z = 15$nm and source wavelength λ 841nm (Fig. 28-29). While an enhancement of 400 is immense, the enhancement remains above 50 well into the Al film. Also, a wavelength λ of 841nm is in the infrared and is not of much interest for applications investigating the visible region of the electromagnetic spectrum.

Only the bowtie mask produced a higher enhancement factor than the novel design for a circularly polarized light source. The novel design generates a maximum enhancement > 40 and confines the largest enhancement factors to a tightly focused volume penetrating into the aperture (Fig. 30).

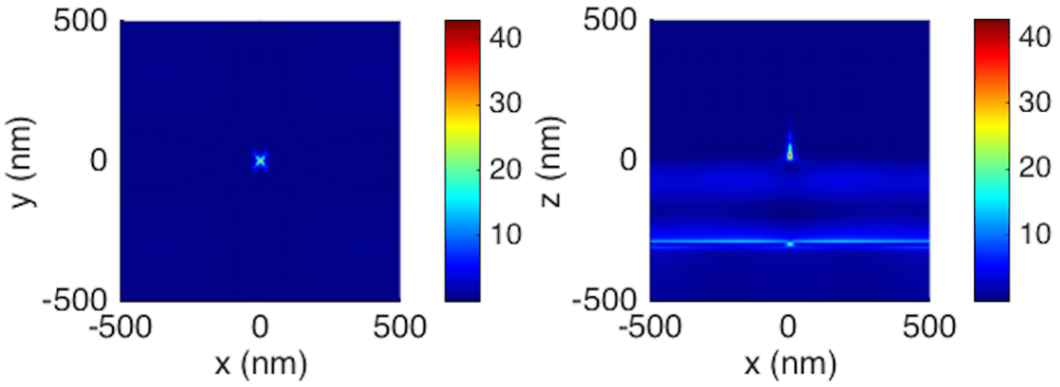

(a) (b)

Figure 30: **Excitation Source Confinement and Enhancement of the Novel Design**. The confinement and enhancement of a circularly polarized light source along the (a) xy-plane and (b) xz-plane.

5 Discussion

One must be sure the thickness of the metal film is of sufficient thickness when designing ZMW consisting of larger aperture dimensions. The red curve in Fig. 31 illustrates the inability to confine light effectively for a ZMW of 100nm thick Al film etched with a bowtie pattern. The metal-stack etched with a bowtie mask produces a high enhancement and also more effectively confines the light within the waveguide than the single Al film with bowtie etch.

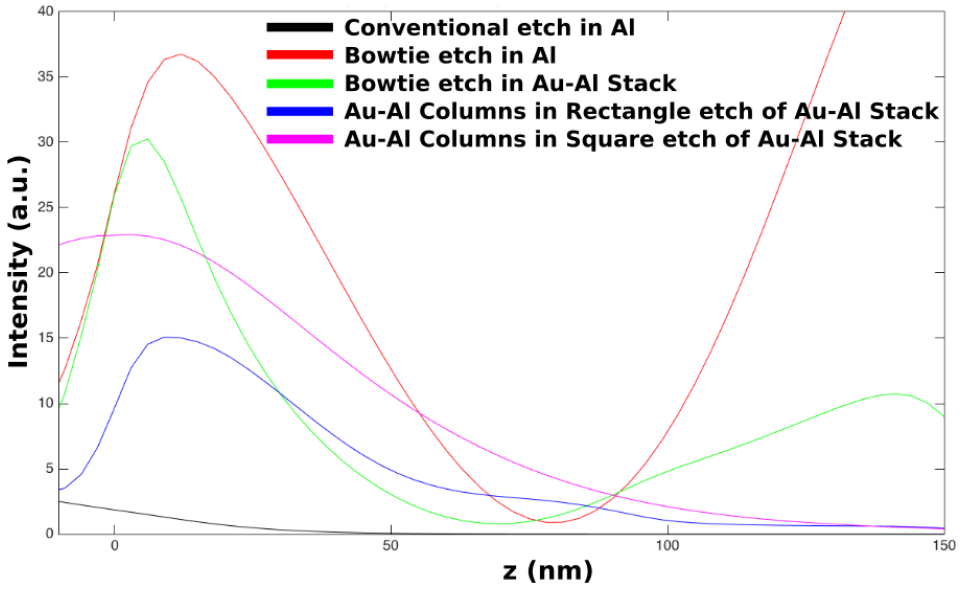

Figure 31: **Comparison of Intensity Enhancement vs Depth**

The novel design consisting of a metal-stack with a custom etch consisting of four columns remaining in a square aperture produced a maximum enhancement of 22.5 with enhancement half-maximum roughly 50nm away from the glass to metal interface. The enhancement of this structure is roughly *two-thirds* less with a half-maximum enhancement depth roughly twice that found for a metal-stack etched with a bowtie. However, once z is greater than 100nm (into the Al film) the signal is enhanced anew.

ZMW devices change behavior with aperture dimension modifications allowing one to design devices to operate at desired wavelengths. If one is interested in a device with a flat frequency response one may do so with a metal-stack with an Al rectangular or bowtie aperture (curves (b) and (d), respectively, in Fig. 32). The metal-stack with a bowtie etch pattern produced an enhancement within 20-30 between the wavelengths of 550- and 850-nm. The ZMW consisting of Al film with rectangular aperture produced enhancements between 10 and 15. If one is interested in a narrow wavelength range one may use a device such as the single Au film or metal-stack with rectangle etch which confine light near 620- and 670-nm, respectively.

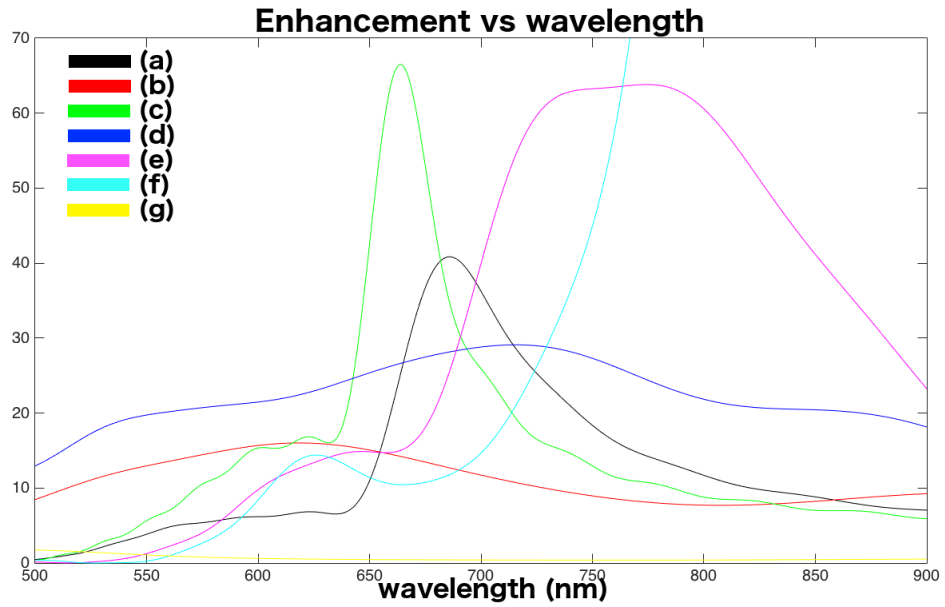

Figure 32: **Wavelength Dependence of Structure Enhancement**. The enhancement at the center of the aperture and z equal to the point of interface between metal and glass for: (a) Au film with rectangular etch, (b) Al film with rectangular etch, (c) metal-stack with rectangle etch, (d) Al with 150nm bowtie etch, (e) 170nm metal-stack with 150nm bowtie etch, (f) 150nm metal-stack with rectangle etch and metal columns in etch and (g) a conventional Al ZMW.

6 Conclusion

Through the study of plasmonic behavior and the computational simulation of the physics involved we were able to compare the enhancement of the radiative decay of quantum emitters. The custom device consisting of a rectangle aperture with metal columns investigated shows promising results to confine light to a volume of $\approx$ 68zL (while also enhancing the signal up to 190$\times$ that of a conventional ZMW (Fig. 28).[6] However, I am left with two questions: (*i*) what is an acceptable signal-to-noise ratio and (*ii*) what is a sufficient intensity from a fluorophore in order for fluorophore detection? While these structures amplify the signal by large amounts — some structures like the Al only film etched with either a rectangle or bowtie also have a nearly flat frequency response which may have a fit in certain applications — I believe the enhancement would become irrelevant after the noise is larger than an

[6]The excitation volume of a square column with a square area of length $2c = 21.2132$nm and height $h = 150$nm. The conventional waveguide would have a volume of 196zL for a circular column of radius $r = 25$nm and height $t = 100$nm. If we change h to the depth at which the enhancement is half of the structure enhancement maximum, $\approx$ 10nm for the conventional waveguide and $\approx$ 40nm for the square column volume, the excitation volumes would be 19.6zL and 18zL, respectively.

amount discernible by detection equipment. The conventional ZMW has a maximum enhancement at the glass-metal interface of roughly 2 and the enhancement decays from there, according to Fig. 29. All the designs studied for this thesis had an enhancement greater than 2 until the depth z from the glass-metal interface was greater than 50nm. While the metal-stack with bowtie etch shows promising results there is much work that needs to be done to confine the light within the aperture (a thicker Al film and thinner Au may produce the desired results). The novel design of a 150nm metal-stack with custom etch pattern (a square aperture with four metal-stack columns) is very promising, however, the machining process will be more difficult than creating a structure in a computer simulation.

References

[1.] P. Bharadwaj and L. Novotny, "Spectral dependence of single molecule fluorescence enhancement", Optics Express, **15**, 21, p. 14266-14274 (2007).

[2.] M. Y. Berezin and S. Achilefu: "Fluorescence lifetime measurements and biological imaging," Chemical Reviews, **110**, 5, p. 2641-2684 (2010).

[3.] M. H. Chowdhury, K. Ray, S.K. Gray, J. Pond, and J.R. Lakowicz: "Aluminum nanoparticles as substrates for metal-enhanced fluorescence in the ultraviolet for label-free detection of biomolecules," Analytical Chemistry. **81**, 4, p. 1397-1403 (2009).

[4.] M. H. Chowdhury, K. Ray, S. K. Gray, J. Pond, J. R. Lakowicz: "The use of aluminum nanostructures as platforms for metal enhanced fluorescence of the intrinsic emission of biomolecules in the ultra-violet," Proc Soc Photo Opt Instrum Eng., **7577**, 75770O, p. 1-9 (2010).

[5.] M. H. Chowdhury, S. K. Gray, J. Pond, C. D. Geddes, K. Aslan and J. R. Lakowicz: "Systematic computational study of the effect of silver nanoparticle dimers on the coupled emission from nearby fluorophores," J Phys Chem C, **112**, 30, p. 11236-11249 (2008).

[6.] M. H. Chowdhury, S. K. Gray, J. Pond, C. D. Geddes, K. Aslan and J. R. Lakowicz: "Computational study of fluorescence scattering by silver nanoparticles, " J Opt Soc Am B, **24**, 9, p. 2259-2267 (2007).

[7.] E. L. Elson: "Fluorescence correlation spectroscopy: past, present, future," Biophysical Journal, **101**, 12, p. 2855-2870 (2011).

[8.] W. M. Haynes: *CRC handbook of chemistry and physics*, (CRC Press, Boca Raton, 2015).

[9.] E. X. Jin and X. Xu: "Enhanced optical near field from a bowtie aperture," Applied Physics Letters, **88**, 153110, p. 1-3 (2006).

[10.] P. B. Johnson and R. W. Christy: "Optical constants of the noble metals," Physical Review B, **6**, 12, p. 4370-4379 (1972).

[11.] C. Kappel. (2012, August 3). *Fluorescence correlation spectroscopy the femtoliter test tube : system calibration and in vitro applications* [Online]. Available:

http://www.leica-microsystems.com

[12.] T. A. Klar, "Biosensing with plasmonic nanoparticles," in *Nanophotonics with Surface Plasmons*, V.M. Shalaev and S. Kawata, Ed. Elsevier (2007).

[13.] J. R. Lakowicz: "Radiative decay engineering 5: metal-enhanced fluorescence and plasmon emission," Analytical Biochemistry. **337**, 2, p. 171-194 (2005).

[14.] J. R. Lakowicz: "Plasmonics in biology and plasmon-controlled fluorescence," Plasmonics, **1**, 1, p. 5-33 (2006).

[15.] J. R. Lakowicz: *Principles of fluorescence spectroscopy* (Springer, New York, 2007).

[16.] M. J. Levene, J. Korlach, S. W. Turner, M. Foquet, H. G. Craighead, W. W. Webb: "Zero-mode waveguides for single-molecule analysis at high concentrations," Science, **299**, p. 682-686 (2003).

[17.] G. Lu, W. Li, T. Zhang, S. Yue, J. Liu, L. Hou, Z. Li and Q. Gong: "Plasmonic-enhanced molecular fluorescence within isolated bowtie nanoapertures," ACS Nano, **6**, 2, p. 1438-1448 (2012).

[18.] S. A. Maier, *Plasmonics: fundamentals and applications* (Springer, New York, 2007).

[19.] D. L. Markovich, K. S. Ladutenko and P. A. Belov: "Performance of fdtd method cpu implementations for simulation of electromagnetic processes," Progress In Electromagnetics Research, **139**, p. 655-670 (2013).

[20.] L. Novotny and B. Hecht, *Principles of nano-optics* (Cambridge University Press, New York, 2006).

[21.] E. Palik and G. Ghosh, *Handbook of optical constants of solids* (Academic Press, San Diego, 1998).

[22.] D. Punj, M. Mivelle, S. B. Moparthi, T. S. van Zanten, H. Rigneault, N. F. van Hulst, M. F. García-Parajó and J. Wenger: "A plasmonic 'antenna-in-a-box' platform for enhanced single-molecule analysis at micromolar concentrations," Nature Nanotechnology, **8**, p. 512-516 (2013).

[23.] B. E. A. Saleh and M. C. Teich, *Fundamentals of photonics* (Wiley, New York, 1991).

[24.] J. B. Schneider, *Understanding the finite-difference time-domain methods*, `www.eecs.wsu.edu/~schneidj/ufdtd`, (2010).

[25.] T. Tanii, R. Akahori, S. Higano, and K. Okubo: "Improving zero-mode waveguide structure for enhancing signal-to-noise ratio of real-time single-molecule fluorescence imaging: A computational study," Physical Review E. **88**, 1, p. 1-5 (2013).

[26.] J. Widengren and Ü. Mets, "Conceptual basis of fluorescence correlation spectroscopy and related techniques as tools in bioscience," in *Single Molecule Detection in Solution*, C. Zander, J. Enderlein and R. A. Keller, Ed. Wiley-VCH (2002).

[27.] K. S. Yee: "Numerical Solution of initial boundary value problems involving maxwell's equations in isotropic media," Antennas and Propagation, **14**, 3, p. 302-307 (1966).

[28.] C. Zhao, Y. Liu, J. Yanga and J. Zhang: "Single-molecule detection and radiation control in solutions at high concentrations via a heterogeneous optical slot antenna," Nanoscale, **6**, 15, p. 9103-9109 (2014).

[29.] MATLAB and Statistics Toolbox Release 2015a, The Mathworks, Inc., Natick, Massachusetts, United States.

[30.] FDTD Solutions, Lumerical Solutions, Inc., Vancouver, British Columbia, Canada.

7 Appendix

7.1 Constants

The constant	Symbol for constant	Rounded value for used
Speed of Light in a vacuum	c_o	$3.0 \times 10^{8}\ m/s$
Planck constant*	h	$6.626 \times 10^{-34}\ m^2kg/s$
Boltzmann constant	k_B	$1.381 \times 10^{-23}\ m^2kg/s^2$K
Elementary electric charge	q	1.602×10^{-19} C
Vacuum Electric Permittivity	ε_0	8.854×10^{-12} F$/m$
Vacuum Magnetic Permeability	μ_0	1.257×10^{-6} H$/m$

Table 1: **Constants Table** *The reduced Planck constant or Dirac constant $\hbar$, is 1.055×10^{-34} m^2kg/s

7.2 Figure of Masks and Metal-Stack Investigated

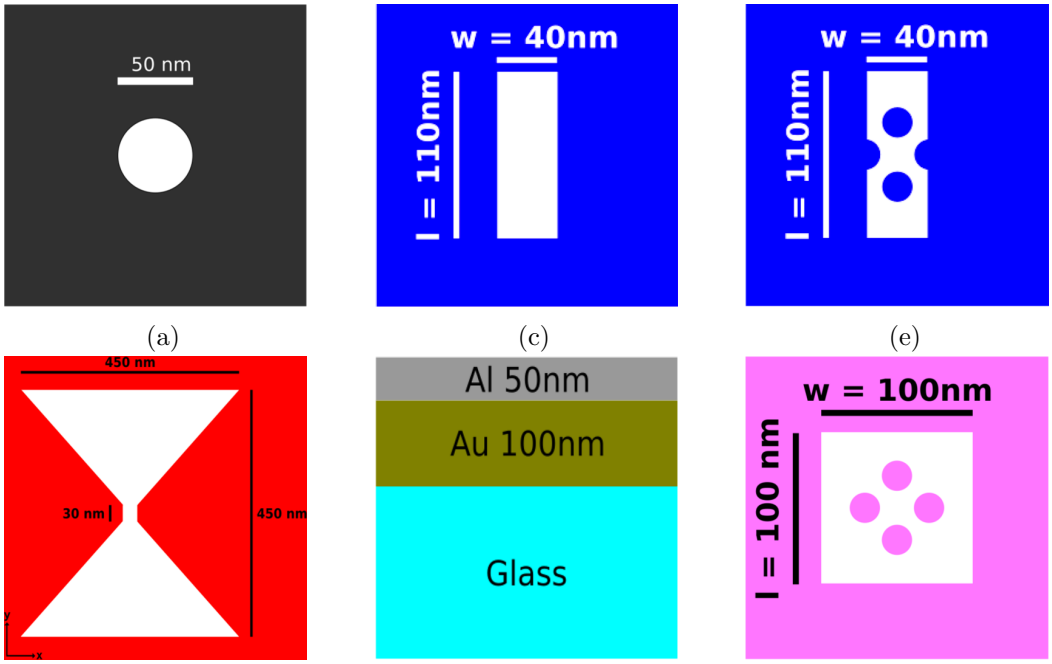

Figure 33: **Aperture Masks and the Metal-Stack**. The etch masks: (a) conventional circular mask with 50nm diameter, (b) a bowtie mask composed of a square of 30nm side length and two right isosceles triangles each with sides 318.2nm long and a 450nm long hypotenuse, (c) a rectangle etch. (d) The metal-stack composed of 100nm of Au and 50nm of Al. Two custom designs (e) a rectangle mask with four metal-stack columns remaining in the aperture space and (e) a square aperture of sides measuring 100nm and four metal-stack columns remaining in the aperture space.